Lawrence Berkeley National Laboratory

Lawrence Berkeley National Laboratory

Title

Binary Pseudo-Random Gratings and Arrays for Calibration of Modulation Transfer Functions of Surface Profilometers

Permalink

https://escholarship.org/uc/item/869330fv

Author

Barber, Samuel K.

Publication Date

2010-01-05

Peer reviewed

eScholarship.org Powered by the California Digital Library University of California

Binary Pseudo-Random Gratings and Arrays for Calibration of Modulation Transfer Functions of Surface Profilometers

Samuel K. Barber,[a] Erik D. Anderson,[a] Rossana Cambie,[a] Wayne R. McKinney,[a]
Peter Z. Takacs,[b] John C. Stover,[c] Dmitriy L. Voronov,[a] Valeriy V. Yashchuk[a,*]

[a] *Lawrence Berkeley National Laboratory, Berkeley, California 94720, USA*

[b] *Brookhaven National Laboratory, Upton, New York, 11973, USA*

[c] *The Scatter Works Inc., Tucson, Arizona 85712*

* E-mail: vvyashchuk@lbl.gov; Phone: +1-510-495-2592; Fax: +1-510-486-7696

ABSTRACT

A technique for precise measurement of the modulation transfer function (MTF), suitable for characterization of a broad class of surface profilometers, is investigated in detail. The technique suggested in [Proc. SPIE **7077**-7, (2007), Opt. Eng. 47(7), 073602-1-5 (2008)] is based on use of binary pseudo-random (BPR) gratings and arrays as standard MTF test surfaces. Unlike most conventional test surfaces, BPR gratings and arrays possess white-noise-like inherent power spectral densities (PSD), allowing the direct determination of the one- and two-dimensional MTF, respectively, with a sensitivity uniform over the entire spatial frequency range of a profiler. In the cited work, a one dimensional realization of the suggested method based on use of BPR gratings has been demonstrated. Here, a high-confidence of the MTF calibration technique is demonstrated via cross comparison measurements of a number of two dimensional BPR arrays using two different interferometric microscopes and a scatterometer. We also present the results of application of the experimentally determined MTF correction to the measurement taken with the Micromap™-570 interferometric microscope of the surface roughness of a super-polished test mirror. In this particular case, without accounting for the instrumental MTF, the surface rms roughness over half of the instrumental spatial frequency bandwidth would be underestimated by a factor of approximately 1.4.

Keywords: Modulation transfer function, MTF, power spectral density, PSD, spatial resolution, surface metrology, surface profilometer, interferometric microscope

1. Introduction

Development and application of state-of-the-art x-ray optics with sub-Angstrom rms roughness and sub-microradian slope variation requires adequate development of surface profilometers and measurement methods [1,2], as well as performance evaluation methods based on rigorous metrology information about the optics. The standard list of output parameters of a profilometer measurement includes values of roughness (residual slope) averaged over an area or along a sample line limited by the bandwidth of the profilometer that is used rather than on the bandwidth required by the particular application [3]. These parameters generally do not provide a sufficient description of the surface that can be used for local finish polishing or for evaluation of the performance of the optic in a particular application. Moreover, the measured surface height (slope) distributions are affected by the instrumental response function, also known as the point-spread function (PSF) [4]. As a result, the measured distribution is a convolution of the ideal surface profile inherent for the surface under test (SUT) with the instrumental PSF. The PSF contains contributions from the instrument's optical system, detector, signal processing, software algorithm, and environmental factors [4]. Generally, these contributions are difficult to account for separately. An additional complication of finding the instrumental response function and corresponding correction of the measurement result arises due to the convolution operation.

In many applications, rigorous information about the expected performance of the optic can be obtained from a statistical description of the surface topography. The description is based on power spectral density (PSD) distributions of the surface height and slope (see e.g., Refs. [5-9] and references therein). For example, the measured PSD distributions provide a closed

set of data necessary for three-dimensional calculations of scattering of light by the optical surfaces [10-12].

Another example is effective combining (stitching) of the metrology data obtained with different profilers. Such a problem appears when characterizing beamline performance of short wavelength (EUV and X-Ray) optics. In this case, in order to cover the wide range of important spatial frequencies from the very low, which affects figure, to the high frequency range, which produces undesirable flare, the metrology from different instruments with significantly different spatial frequency bandwidths needs to be combined into a single global measurement [9]. Analysis in the spatial frequency domain is necessary because correction of instrumental distortions is more straightforward in the frequency domain rather than in the spatial domain. Indeed, a convolution in the spatial domain is equivalent to a multiplication in the spatial frequency domain, which is a far simpler process.

In the spatial frequency domain the PSF is related to the optical transfer function (OTF). The OTF is generally a complex function comprised of a magnitude and phase portion, known as the modulation transfer function (MTF) and phase transfer function (PTF), respectively [4]. In the course of PSD measurement, the surface PSD is obtained by the square modulus of a straightforward discrete Fourier transform of the measured height distribution. Thus the phase portion of the OTF drops out which provides the following relation:

$$PSD_{measured} = PSD_{SUT} \times MTF^2 . \quad (1)$$

The MTF in Eq. (1) is the total MTF of the instrument and, to the extent that the response of the instrument can be characterized as a linear system, is a product of the MTFs of the individual components (objective, detector, etc.) of the instrument. As such, it suggests a simple method to experimentally determine the instrumental MTF. The MTF can be determined by comparing the PSD distribution measured with a known test surface to the corresponding ideal PSD distribution which is numerically simulated. The square root of the ratio of the measured PSD distribution to the simulated PSD distribution gives the MTF of the instrument.

The effectiveness of this experimental method for MTF calibration hinges critically on the appropriate choice of a test surface. First of all, a successful test surface should provide a calibration over the entire instrumental field of view. Second, the surface should provide MTF calibration with equal efficiency over the entire spatial frequency range up to the Nyquist frequency of the instrument. Most of the common test patterns used in MTF measurements, including knife-edge sources (step height standards) [13-17], bar targets [18], sinusoidal [19] and periodical patterns [20,21], do not meet these requirements. Additionally, in order to be used as a certified standard, the MTF test surface should meet the condition of ease of specification, reproducibility, repeatability, and reasonably low sensitivity to possible fabrication imperfections. The white noise patterns [22] and random reference specimens [21,23] suggested and developed so far do not satisfy this condition. For a comprehensive review of the standard reference specimens, see Ref. [24] and references therein.

In the present work, we investigate in detail a technique for precise measurement of MTF, suitable for characterization of a broad class of surface profilometers. The technique suggested in Refs. [25,26] is based on use of binary pseudo-random (BPR) gratings and arrays as standard MTF test surfaces. Unlike most conventional test surfaces, the inherent PSD of the BPR gratings and arrays has a deterministic white-noise-like character. This allows the direct determination of the one- (1D) and two-dimensional (2D) MTF, respectively, with a sensitivity uniform over the entire spatial frequency range of a profiler. The high efficiency of using BPR gratings (BPRGs) as a standard 1D test surface for measurement of the 1D MTF of a Micromap^{TM}-570 interferometric microscope has been experimentally demonstrated [25,26].

1 In the present work, a demonstration of the 2D MTF calibration technique is presented via 2 cross comparison measurements of a number of two dimensional BPR arrays (BPRAs) using 3 two different interferometric microscopes and a scatterometer. We also present the results of 4 application of the MTF correction, experimentally determined with the technique using BPR 5 arrays, to the measurement of the surface roughness of super-polished test mirrors with the 6 Micromap^{TM}-570 interferometric microscope.

7 This paper is organized as follows. In the next section, we provide the mathematical 8 fundamentals of BPR sequences and arrays that are important for the MTF measurements. 9 Section 3 briefly discusses the main techniques used to fabricate the BPR test surfaces. In 10 Section 4, investigation of the correlation properties of the BPRA test surfaces with a 11 scatterometer are described. The details of the MTF calibration of two interferometric 12 microscopes, Micromap^{TM}-570 and ZYGO NewView^{TM}-6300, as well as a few examples of 13 application of the calibration to the measurements with high quality optics are given in 14 Section 5. The paper concludes by summarizing the main concepts discussed throughout the 15 paper and stating a plan for extending the technique to calibrate other types of surface 16 profilometers.

17 ## 2. Fundamentals of BPR sequences and arrays

18 BPR sequences and arrays are one- and two- dimensional patterns of binary elements, e.g., 1's 19 and 0's or -1's and +1's, in which the elements appear statistically independent and uniformly 20 distributed. The term 'pseudo-random' implies that the distributions are generated by 21 mathematically precise rules to possess a property of randomness in the mathematically strong 22 sense [27-29]. Although we have chosen the term "pseudo-random sequence," such sequences 23 are alternatively referred to as pseudo-noise sequences or m-sequences [27].

24 Particular methods for generation of pseudo-random sequences [30,31] were developed in 25 connection with communication and encryption processes (see, e.g., Ref. [32] and references 26 therein), acoustics [33], and for pseudo-random chopping of a beam in time-of-flight (TOF) 27 experiments with slow neutrons [34-39] and molecular beams [40-42]. In TOF experiments, 28 the sequences are mathematically represented with 1's, which denote an open chopper slot, 29 and 0's, which denote a closed chopper slot. The chopping associated with a cross-correlation 30 analysis of the measured time-resolved detector signal is favored over single-shot (periodic) 31 chopping with duty-cycle gain factor as high as $N/4$ (assuming two slits on a periodic 32 chopper), where N is the length of the pseudo-random sequence, without loss of resolution. 33 The maximum duty cycle (relative number of 1's and 0's) of approximately 50% is obtained 34 with a maximum-length pseudo-random sequence (MLPRS) [31,40,41].

35 To be qualified as a MLPRS, a sequence $\{a_i\}$ of N elements ($i = 0,1,\cdots,N-1$, $N = 2^n - 1$, 36 where n is an integer) must obey two conditions for its correlation function. First, the 37 autocorrelation of the sequence must sum to 2^{n-1}. That means that the cyclical correlation 38 functions of the sequence, which is determined as

39 $$A_j = \sum_{i=0}^{N-1} a_i a_{i+j}, \quad j = 0,1,\cdots,N-1, \qquad (2)$$

40 sums to $A_0 = 2^{n-1}$ (equal to the number of 1's in the MLPRS) at $j = 0$. Second, the sequence 41 has to be 'almost' uncorrelated, which means that the cross-correlation of the sequence, A_j at 42 $j \neq 0$ all are equal to each other, $A_j = 2^{n-2}$. The conditions are very natural if one uses a 43 definition of a purely random sequence, or white noise, as a sequence which consists entirely 44 of uncorrelated binary elements with a δ-function-like correlation function. According to the

Wiener-Khinchin theorem [43], the PSD of a sequence with a δ-function-like correlation function is a frequency-independent white-noise-like distribution.

Two-dimensional analogues to the BPR sequences considered above are uniformly redundant arrays (URA). URAs are widely used as optimum mask patterns for coded aperture imaging techniques (for review, see Ref. [28] and references therein). Analogous to the TOF technique based on 1D BPR sequence chopping, 2D URA-based imaging, when applied to x-ray and gamma ray astronomy and x-ray holography, allows one to obtain a better signal-to-noise ratio, keeping the high angular resolution characteristic of a single pinhole aperture [44-46].

The URA's superior imaging capability originates from the fact that URAs possess both high throughput (50%) and a delta-function-like cyclical autocorrelation function that corresponds to a flat 2D PSD spectrum. Tracking the mentioned similarity of the binary pseudo-random sequences and uniformly redundant arrays, we employ the terms BPR grating and BPR array rather than URA for the latter one, when discussing the test surfaces used for the MTF calibration. The URA used in this paper follows the original prescription of the twin-prime class given in Ref. [44]. The URA is configured as a rectangular aperture of dimensions $r \times s$, where r and s are prime numbers and $r = s + 2$. For more details on the URA generation algorithm see Refs. [44,45].

For MTF calibration of surface profilometers, we designed 1D and 2D BPR gratings and arrays which are sets of rectangular grooves pseudo-randomly distributed over a uniform 1D and 2D grid, respectively. Figure 1 illustrates the design. The pitch of the grid determines the width of the smallest element of the pattern (fundamental period) and, therefore, the inherent Nyquist frequency of the BPR pattern. The BPR patterns generated with a maximum filling factor of about 50% provide improved signal-to-noise ratios of the PSD spectra of the test surface. The inherent PSD spectrum of such a grating is independent of spatial frequency (white-noise-like). Therefore, any deviation of a PSD spectrum measured with a real instrument from a white-noise-like spectrum would be a measure of the instrumental MTF. Note that the PSD from a BPR grating or array is a result of the groove distribution and is not particularly sensitive to the groove shape or roughness of the groove surfaces, top and bottom [25,26].

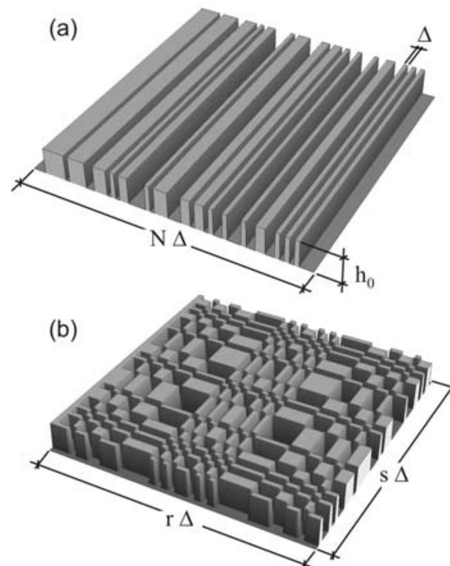

Figure 1: Examples of BPR test patterns: (a) 1D BPR grating of 63 grooves and (b) 2D BPR array of 43×41 elements. In order to generate the BPR patterns, the algorithms described in Refs. [31] and [44] were used.

3. **Fabrication of the BPR gratings and arrays**

Due to the deterministic binary character, the BPR test surfaces are easy to specify for standard micro- and nano-fabrication processes. For the purpose of MTF measurement, an ideal surface based on a BPR pattern is determined as a set of rectangular grooves of binary height levels with grooves and peaks corresponding to values of 1 and 0 in the BPR sequence or array (Fig. 1). The optimal height, h_0, and fundamental element size (pitch), Δ, depend on the specifics of the instrument under calibration.

The value of Δ effectively determines the Nyquist spatial frequency of the test surface, $f_N = 1/(2\Delta)$. This is the frequency up to which the inherent PSD of the BPR test surface is expected to be flat. The lower bound is determined by the total size of the surface, which is equal to the product of Δ and the number of columns/rows in the BPRA, $f_{0,x} = 1/(r \cdot \Delta)$ and $f_{0,y} = 1/(s \cdot \Delta)$ for the x- and y- directions, respectively.

For an effective MTF measurement over the entire spatial frequency range of the instrument, the test surface bandwidth should sufficiently cover that of the instrument. The value of f_N should be larger than the Nyquist frequency of the instrument under test in order to avoid sinc-function-like behavior of the test surface PSD at frequencies higher than f_N. If the BPR test surface does not fill the entire field of view of the instrument, an extra contribution in the measured PSD will appear due to a gate-function-like surface feature with the aperture of $(r \cdot \Delta) \times (s \cdot \Delta)$ and the height of $h_0/2$. In order to avoid this effect, the test sample should be fabricated as a three level structure: $-h_0/2$ and $+h_0/2$ levels for the BPR pattern and zero level for the entire surface. Taking into account that the fabrication process should guarantee the zero surface level to be exactly on the middle between the lower and the upper levels of the pattern, such a structure is significantly more difficult to fabricate.

For the present work, one of the instruments in question is the Micromap^{TM}-570 interferometric microscope. The microscope has a 640×480 pixel imaging CCD camera and can be equipped with five objectives, 2.5×, 5×, 10×, 20×, and 50×. The corresponding effective pixel sizes (sampling intervals) determined by the objective in place are 3.92 μm, 1.96 μm, 0.98 μm, 0.49 μm and 0.192 μm. Therefore, the smallest pitch of a BPR pattern should be about 200 nm. However, a conventional lithographical process, which was used for fabrication of the BPR gratings used in Refs. [25,26], is suitable only for $\Delta \geq 2\,\mu$m.

The prototype BPR array samples of 4021×4019 elements which required small pitches were fabricated by using the nanolithograthy facility available at the Center for X-Ray Optics of the Materials Science Division, LBNL [47]. High-resolution electron beam lithography and Induction Coupled Plasma (ICP) etching into a silicon substrate were specially optimized for this purpose. The BPR array was generated using the algorithm described in Ref. [44]. The 1’s in the array correspond to rectangular grooves in the substrate and 0s represent peaks, or portions that are not etched.

The first set of nine prototypes, with fundamental element sizes of 200 nm, 400 nm, and 600 nm etched into a silicon (100) wafer to different depths: 49 nm, 63 nm, and 122 nm, has been investigated in Ref. [48]. The etch chemistry that was used, which was based on SF_6 and Ar, was found to be reliable and fast but did not produce vertical sidewalls – Figs. 2a and 3a. However, the fabrication imperfection only slightly affects the shape of the inherent PSD of the test sample, leading to an approximately 10% roll off at higher spatial frequencies. Moreover, the correction method developed in Ref. [48] allows for analytic accounting of the perturbation based on the profile measurements taken with a scanning electron microscope (SEM), Fig. 2, and a scanning probe microscope (SPM), Fig. 3.

Further optimization of the BPRA fabrication by using 100 KeV electron beam lithography was made [49] to generate better vertical sidewall profiles. Figures 2b and 3b show the SEM and SPM micrograph of the HBr etched BPRAs. The sidewall is essentially vertical-producing near ideal structures for a test sample. No evidence of feature-size-etch-dependent etch rates were observed at the dimensions of interest. The optimum etch depth is approximately 103 nm. BPRA patterns with three fundamental sizes of 200 nm, 400 nm, and 600 nm were fabricated. Additional information regarding the fabrication of these BPRA samples can be found in Ref. [49]. These samples are used throughout the present work.

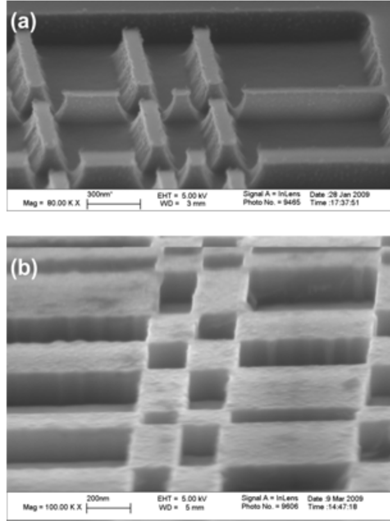

Figure 2: SEM micrographs of a part of 200 nm BPR arrays fabricated using (a) SF_6/Ar etch and (b) HBr etch. Notice the near 90 degree sidewall slope and the squareness of the tops of the peaks in (b). These features are in line with what is considered, for our purposes, an ideal array.

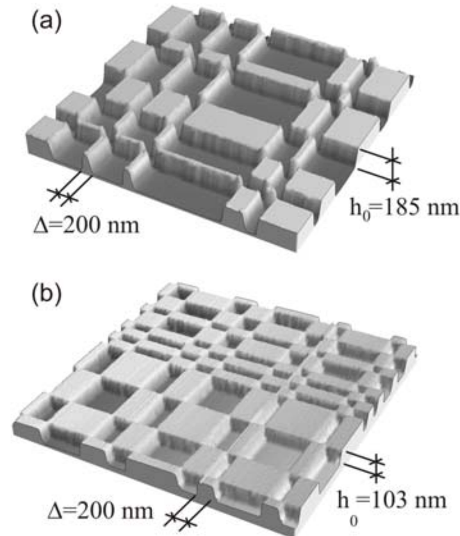

Figure 3: 5 μm × 5 μm SPM scans of the BPR arrays fabricated using (a) SF_6/Ar etch and (b) HBr etch. The SF_6/Ar etch array is the same as one shown in Fig. 2a. The extension-like sidewall perturbation clearly seen on the 600 nm HBr etch array is an artifact of the SPM measurement. It was found by flipping the sample by 180º and re-measuring. The perturbation locations were not altered by flipping of the sample.

4. **Scatterometer measurements with BPR arrays**

Correlation properties of the HBr etched BPR arrays with 200 nm, 400 nm, and 600 nm minimum feature size were verified by measuring the bidirectional reflectance distribution function (BRDF) [11] with a CASI™ scatterometer [50] at the Scatter Works (TSW Inc.) [51].

The physical meaning of the BRDF is a ratio of the differential radiance to the differential irradiance [11]:

$$BRDF \equiv \frac{P_s / \Omega_s}{P_i \, Cos\,\theta_s}, \tag{3}$$

where P_s and P_i are the scattered and incident light fluxes, respectively; Ω_s is the scattered solid angle, and θ_s is the polar scatter angle measured from the surface normal. Based on the Rayleigh-Rice vector perturbation theory [10,11], one can relate the BRDF to the surface 2D PSD function $S(f_x, f_y)$:

$$BRDF = \frac{16\pi^2}{\lambda^4} Cos\,\theta_i \, Cos\,\theta_s \, \Theta \, S(f_x, f_y), \tag{4}$$

where the dimensionless quantity Θ is the reflectivity polarization factor that for the case of an S polarized source can be approximated by the sample reflectance, and θ_i is the incidence angle. Therefore, the scatterometer measurements provide an independent characterization of the inherent PSD distribution of the BPR arrays.

The CASI™ scatterometer used for these measurements operates with several different lasers (with wavelengths of 488 nm, 633 nm, 830 nm, and 980 nm) and variable source/receiver polarization configurations. It measures incident plane scatter at most incident angles and can make limited out-of-plane measurements. For the measurements described below the 488 nm wavelength light source was used.

Figure 4 shows a simplified schematic of the CASI™ scatterometer.

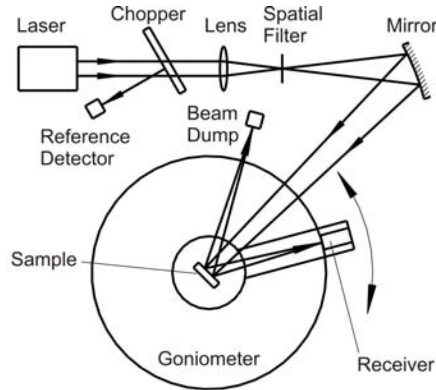

Figure 4: Schematic of the experimental set-up of the CASI scatterometer [50].

A receiver placed on a precise goniometer stage can be moved in the plane of incidence, providing angle sensitive detection of the scattered light. In order to put the receiver in the far field region, the incident beam is usually focused with a mirror, so that the light reflected from the sample is focused on the receiver aperture. The receiver has four different sized apertures. A 300 µm aperture is used close to specular; and the largest aperture (approximately 14 mm) is used far from the specular reflection. Aperture change, angles, and step sizes are programmable. An automatic change of the electronic gain and source neutral density filter, as well as the aperture, allows for covering 14 orders of magnitude of dynamic range of BRDF

measurements as the receiver angle scans through the specular reflection into the wings of the grazing scatter. The BRDF noise floor is about 10^{-8} sr^{-1} with a silicon diode detector and 10^{-10} sr^{-1} with a PMT.

In the course of measurements with the BPR arrays, the source angle of incidence was at a near-normal angle of 5º. The measurements were made with the samples oriented so that one axis of the grid pattern was in the plane of incidence with the detector angle scanned between ±90º relative to the surface normal. In this arrangement, the measured BRDF is basically an average of the plane-of-incidence slices of the 2D PSD that is equivalent to the 1D PSD in the slice direction.

The BSDF curves for all three patterns are shown in Fig. 5. The two peaks in the wings of the scatter curves are from the first order diffraction from the 600 nm fundamental period for the 488 nm illumination wavelength.

The corresponding 2D PSD curves shown in Fig. 6 are the result of computation from the BRDF curves using Eq. (4). The PSDs from the negative angles are folded over into the positive frequency domain so that both branches are plotted on the same positive frequency axis. The PSD curves are essentially flat over most of the spatial frequency range, indicating that these BPR arrays do indeed perform as a white noise surface.

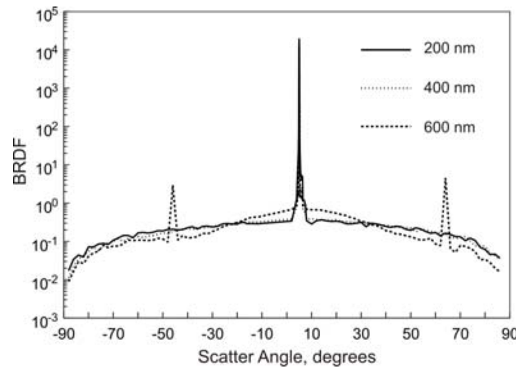

Figure 5: Scatterometer BRDF measurements on each of the three patterns at a 488 nm illumination wavelength. First order diffraction from the 600 nm pattern feature size is evident in the corresponding curve.

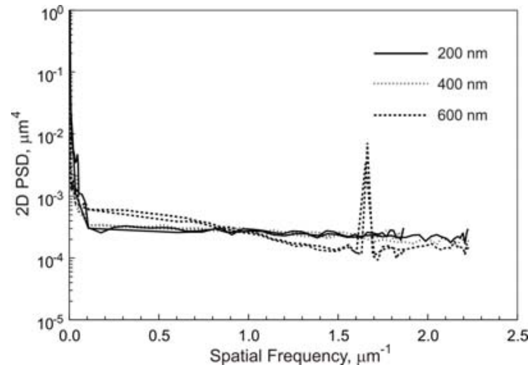

Figure 6: Reduced 2D PSD curves computed from the BRDF for the three patterns. Negative scatter angles are folded over to positive frequencies. The nearly-horizontal lines indicate the white-noise nature of the BPRA.

5. MTF correction of PSD measurements with interferometric microscopes

The Br-etched BPRA samples described above were used as standard test surfaces for MTF calibration of the MicroMap^{TM}-570 and ZYGO NewView^{TM}-6300 interferometric

microscopes. The MTF test samples of 4021×4019 elements were etched to have the structure depth of about 103 nm (see Sec. 3). The depth is a compromise between two opposite limitations. First, the depth should be significantly larger than the substrate (wafer) surface variations as discussed in Ref. [49]. Second, the depth should be small enough in order to avoid any possible nonlinear effects of the PSD measurements with the BPR test sample and, therefore, the MTF calibration.

Figure 7 presents the MicroMap™-570 PSD measurements with three test samples with depth h_0 of 49 nm, 63 nm, and 122 nm. The 1D PSD spectra were directly calculated from the measured height distributions without using any correction. For PSD calculation, we use the same discrete PSD algorithm as the one described in Refs. [7-9]. In order to decrease the speckle noise, the 2D PSD spectra of the height distributions measured over four different subsets of the BPR pattern, each shifted successively by approximately 400 pixels, were averaged.

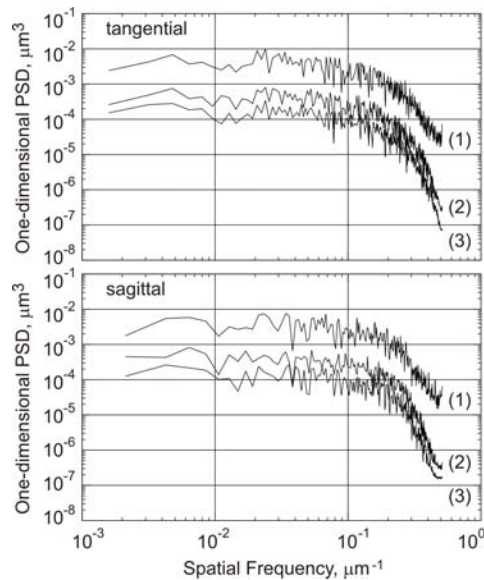

Figure 7: Tangential and sagittal 1D PSD spectra of the BPRAs with 400 nm elementary step and different depth: (1) 122 nm, (2) 63 nm, and (3) 49 nm. Measurements were made with the MicroMap™-570 microscope equipped with the 10× objective.

The remarkable observation is that the shape of the PSD spectra does not significantly depend on the depth of the samples. This can be thought of as evidence for linearity of the interferometric microscope measurements (at least when using incoherent light) with the 2D BPR structure with depth up to approximately 100 nm. Note that even more strong evidence for linearity of PSD measurements with BPR test surfaces has been obtained with a BPR grating with an etch depth of approximately 700 nm [25,26]. In this case, the effective depth of the grating seen by the Micromap™-570 was only 174 nm. The discrepancy was attributed to the uncertainty of 2π of the phase-retrieval algorithm of the instrument with the light wavelength of $\lambda \approx 520$ nm. As pointed out in Refs. [25,26], this circumstance did not compromise the possibility to calibrate the instrument if the 2π phase shift due to the retrieval was applied to the entire measured surface. Note that the dependence of the MTF calibration on the BPRA pitch has been investigated in Ref. [48]. It was demonstrated that for the Micromap™-570 equipped with the 10×, 20× and 50× objectives, the MTFs determined by using the 200 nm, 400 nm and 600 nm BPRAs etched to 63 nm depth are identical.

1 Below we describe the calibration procedure and provide a few examples to demonstrate how
2 the calibration affects the final result of the SUT metrology. We also compare the result of the
3 MTF calibration performed with the 2D BPR-pattern-based method and other methods
4 applied to the same instrument [7]. Here, we only mention that the calibration results are in
5 excellent agreement.

6 5.1. MicroMap^{TM}-570 interferometric microscope

7 Figure 8 shows representative MicroMap^{TM}-570 height data for the 400 nm Br-etched BPRA
8 sample with depth of 103 nm. Note that the measurement performed with 10× objective
9 provides the rms roughness of about 9.7 nm that is significantly below the inherent rms
10 roughness of the sample of $h_o = 51.5$ nm.

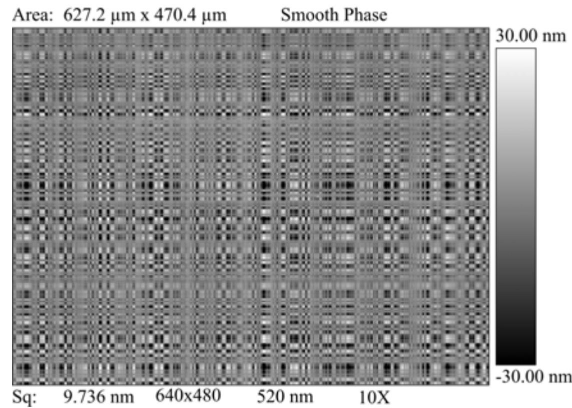

11

12 Figure 8: A section of the 400 nm BPR array with 103 nm depth measured with
13 Micromap^{TM}-570 interferometric microscope equipped with 10× objective. The
14 microscope field of view of 627.2 µm × 470.4 µm is imaged with 640 pixels ×
15 480 pixels.

16 Besides the resolution of the instrument, the measured roughness of the sample depends on
17 the undersampling effect due to the instrument pixel size of 0.98 µm. For real experimental
18 arrangements, when an instrument with finite detector pixel size is used, one can not expect
19 the grid of the BPR array projected onto the detector to line up exactly with the boundaries of
20 each detector pixel. Moreover, in the general case, the grating pattern is undersampled and the
21 pixel area encompasses more than one array element.

22 In order to account for the under-sampling effect, we simulate the height distribution seen
23 with an ideal microscope with a pixel size corresponding to the used objective that is larger
24 than the pitch of the BPRA. In this case, assuming linearity of the measurements, the height
25 value seen in a given pixel can be modeled by averaging over the height of the BPRA
26 elements (or the area parts of the elements) covered by the pixel. Application of the procedure
27 to the measurement shown in Fig. 8 provides an undersampled height distribution with a
28 reduced rms roughness of 17.6 nm, which is still larger than the measured one. As shown
29 below, the rest of the difference is due to the instrumental MTF.

30 The under-sampled height distribution of the BPRS can be used in order to evaluate its
31 inherent (theoretical) 2D PSD distribution. For the experimental arrangement corresponding
32 to Fig. 8, the theoretical tangential and sagittal 1D PSD distributions obtained this way are
33 presented in Fig. 9 together with the rough 1D PSD measured with the microscope. Because
34 the high quality of the BPRA sample under test, the low spatial frequency level of the
35 theoretical and experimental spectra is the same. Therefore, in order to get the MTF
36 calibration of the instrument, it is enough to directly use Eq. (1) assuming a flat inherent PSD
37 with an amplitude corresponding to the calculated rms roughness of 17.6 nm.

1

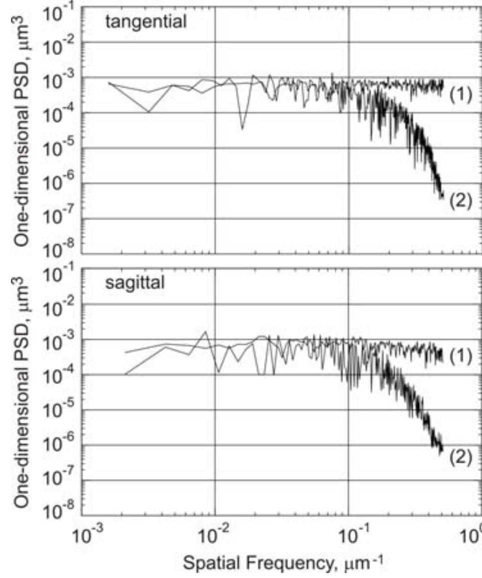

2 Figure 9: (1) Theoretical 1D PSD distributions of the 400 nm BPRA and the
3 corresponding 1D PSDs measured with the Micromap[TM]-570 microscope
4 equipped with 10× objective. The roughness from the theoretical PSD is 17.6
5 nm (rms); the experimental roughness measured over the same frequency range
6 is 9.7 nm (rms) – compare with Fig. 8. In order to suppress the variation of the
7 spectra, averaging over four measurements with shifted BPRA sample was
8 performed. A similar approach was used to calculate the theoretical PSD.

9 The described *ab initio* MTF calibration can be compared with the previous empirical
10 calibration of the same instrument performed a few years ago [7]. Unfortunately, a direct
11 comparison became impossible because from that time the instrument software has been
12 upgraded from the version 4 to the version 5. As it was experimentally determined, the new
13 software includes additional averaging over each two neighbor tangential pixels. The
14 averaging was, probably, included in order to fix an asymmetry of the read-out process of the
15 Micromap[TM]-570 detector described in Ref. [7]. As a result, with the new software the
16 effective resolution of the instrument has been reduced and the correction procedure applied
17 in Ref. [7] should be reconsidered. The additional averaging can be accounted with an
18 analytical expression analogous to one derived in [7] for the detector pixel MTF:

19
$$MTF_P(f_x, f_y) = \left(\frac{Sin\pi\, p_x \Delta x\, f_x}{\pi\, p_x \Delta x\, f_x}\right)\left(\frac{Sin\pi\, p_y \Delta y f_y}{\pi\, p_y \Delta y\, f_y}\right) Cos^{-1}\left(\pi\,\Delta x\, f_x\right) Cos^{-1}\left(\pi\,\Delta y\, f_y\right), \qquad (5)$$

20 where f_x and f_y are the components of the spatial frequency, Δx and Δy are the nominal
21 detector pixel sizes, $p_x \Delta x$ and $p_y \Delta y$ are the effective pixel sizes projected on to the surface
22 plane. The sinc function multiplicands in Eq. (5) present the instrumental MTF associated
23 with sampling with finite pixels (see, e.g., Ref. [52]). The cosine multiplicands depict the
24 averaging over two neighbor pixels. Another primary MTF effect that should be also
25 accounted in the analytical expression for the MTF is that of the lens aperture. The MTF for a
26 diffraction-limited objective with incoherent illumination is given by [52,53]

27
$$MTF_O(f) = \frac{2}{\pi}\left[-\Omega\sqrt{1-\Omega^2} + ArcCos\,\Omega\right], \qquad (6)$$

where $\Omega = \lambda f / 2NA$, λ is the measuring wavelength, $\lambda = 520$ nm, $f = \sqrt{f_x^2 + f_y^2}$, and NA is the numerical aperture; $NA \approx 0.3$ for the 10× objective. The result of application of the corrections (5) and (6) with an optimal effective pixel size of 1.96×1.96 μm^2 is shown in Fig. 10. In this case, the corrected PSD flattens out to a noisy horizontal line, becoming a white-noise-like spectrum, indicating that the applied MTF corrections are sufficient to account for the observed high-frequency roll-off. The resulting analytical MTF correction is in an excellent agreement with the result obtained in Ref. [7].

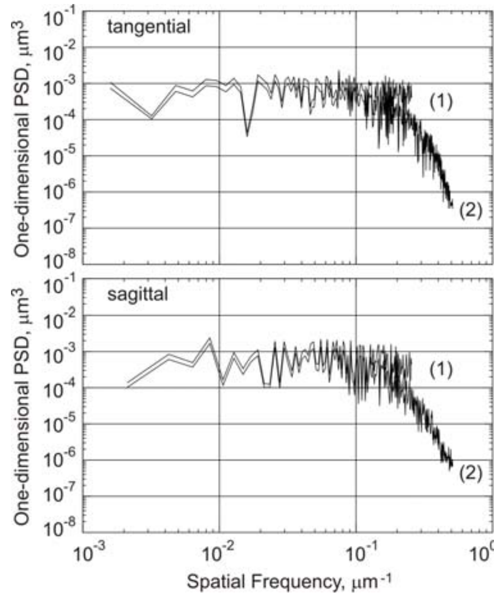

Figure 10: (1) The 1D PSD distributions of the 400 nm BPRA after the analytical correction procedure based on Eqs. (5) and (6) was applied to the measured PSD distribution (2). Only one parameter $p = p_x = p_y \approx 2.0$ was determined by fitting. All the calculations were performed with the 2D PSD and 2D MTF distributions, which were finally converted to the 1D distributions shown in the figures.

Note that the corrected PSD distributions are presented with a significantly decreased bandwidth that accounts for the real Nyquist frequency of the instrument with increased effective pixel size. The sample surface roughness evaluated even over the decreased bandwidth of the corrected PSD is 13.5 nm (rms) that is factor of 1.4 smaller of that of obtained directly from the Micromap™-570 measurement shown in Fig. 8. Therefore, the MTF correction allowed us to define the correct bandwidth of the instrument and provide a much more reliable surface roughness over the actual bandwidth.

A similar result is obtained when the MTF correction is applied to the measurements with a SUT rather than with BPR test sample. Figure 11 shows a printout of the MicroMap™-570 height data obtained with a super polished aluminum mirror [54]. The measurement was performed with 10× objective and provided the rms roughness of ~1.6A.

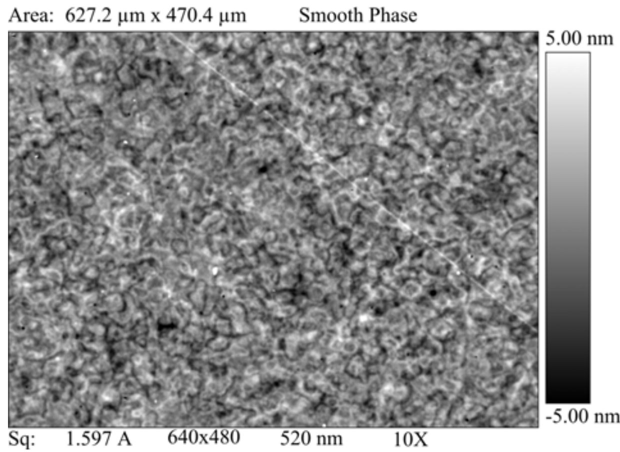

Figure 11: Surface height distribution of a super polished aluminum mirror [54] measured with the Micromap^{TM}-570 interferometric microscope equipped with 10× objective. The surface roughness value evaluated from the distribution is 1.6 A.

The MTF-corrected and uncorrected 1D PSD distributions corresponding to the measurement in Fig. 11 are presented in Fig. 12. The MTF correction applied is the same as one described above and used to get the PSD data shown Fig. 9. The rms roughness estimated from the corrected PSD with decreased frequency bandwidth is 2.2 Å that should be compared with value 1.6 Å corresponding to the uncorrected measurement.

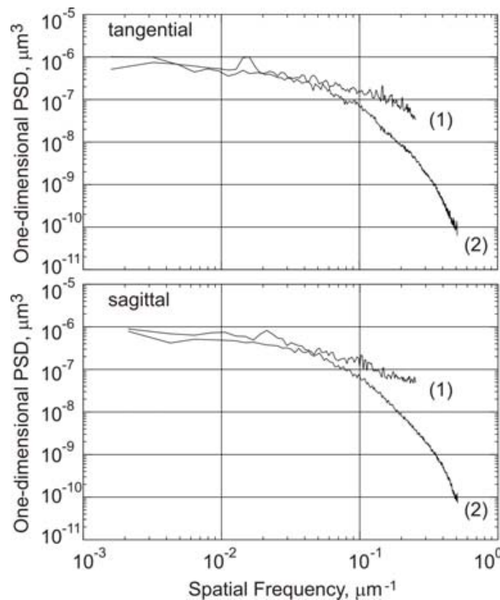

Figure 12: (1) The 1D PSD distributions of a super polished Al mirror after the analytical correction procedure based on Eqs. (5) and (6) was applied to the measured PSD distribution shown with the plot (2).

5.2. ZYGO NewView ^{TM}-6300 interferometric microscope

Measurements were made on the 103 nm depth BPR arrays with a Zygo NewView^{TM}-6300 interferometric microscope. Measurements were made on all three patterns that have fundamental period of 200 nm, 400 nm, and 600 nm respectively, with two different objective magnifications: 20× and 2.5×. In both cases the internal zoom lens was set at 1x magnification. The combination of objective lenses with the 640×480 pixel detector provides the range of sampling parameters indicated in Table I. The BPR arrays contain the intrinsic spatial frequency parameters shown in Table II.

Table I - NewView ^{TM}-6300 system parameters

Objective	Lens NA	Pixel size [µm]	fNy, Nyquist frequency, [µm^{-1}]	Lens MTF cutoff frequency [µm^{-1}]
20×	0.40	0.548	0.912	1.403
2.5×	0.075	4.385	0.114	0.263

Table II – Intrinsic BPRA parameters.

Fundamental period, d	Feature frequency, 1/d [µm^{-1}]	Feature Nyquist frequency, 1/2d, [µm^{-1}]
600 nm = 0.6 µm	1.667	0.833
400 nm = 0.4 µm	2.50	1.25
200 nm = 0.2 µm	5.00	2.50

All of the pattern grids were aligned with a slight angular misalignment to the grid coordinate system defined by the detector. The detector under-sampled the frequency content of each array except for the 20×-600 nm pattern combination, where the detector Nyquist frequency extended just beyond the feature Nyquist frequency. The detector field of view (FOV) was smaller than the magnified pattern image area in all cases except for the 2.5×-400 nm and 2.5×-200 nm combinations. In these cases, the flat regions outside the etched areas were excluded from the PSD calculation. This imposes a different low-frequency cutoff on the PSD, but does not affect the high frequency characteristics. The average PSD for each measured area was calculated by first detrending each row in the array by removing the mean, then computing the 1D PSD for each row and averaging the resulting PSDs. Then the MTF correction factors were applied according to Eqns. (5) and (6), but without the need to invoke an asymmetric x and y pixel size correction, as the NewView does not average pixels in the y-direction. The tangential and sagittal PSDs are the same for this surface. In this case, (5) simplifies to just the first term on the right side with $p_x = 1$. The results of the PSD calculations for the 20× measurements are shown in Fig. 13 and for the 2.5× measurements in Fig. 14.

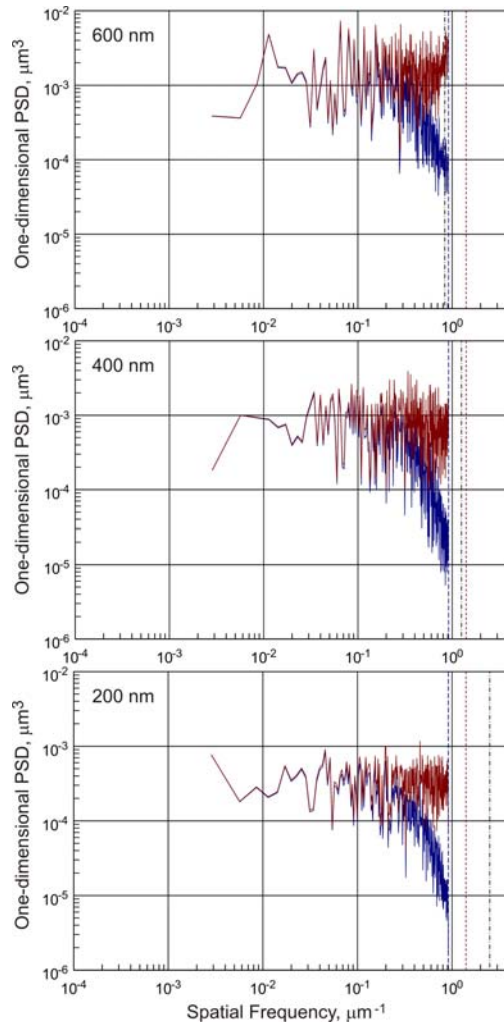

1

2 Figure 13: Average 1D PSDs for the 20× NewView measurements on each
3 BPRA pattern. Lower curve is uncorrected, upper curve is corrected for
4 instrumental MTF. The corrected PSDs are flat and horizontal as they should
5 be for a white-noise-like surface height distribution. Vertical lines indicate
6 frequency cutoffs according to the above tables. The long-dash line
7 corresponds to the detector Nyquist frequency; the short-dash depicts the lens
8 cutoff; the dot-dash line shows the BPRA feature Nyquist frequency.

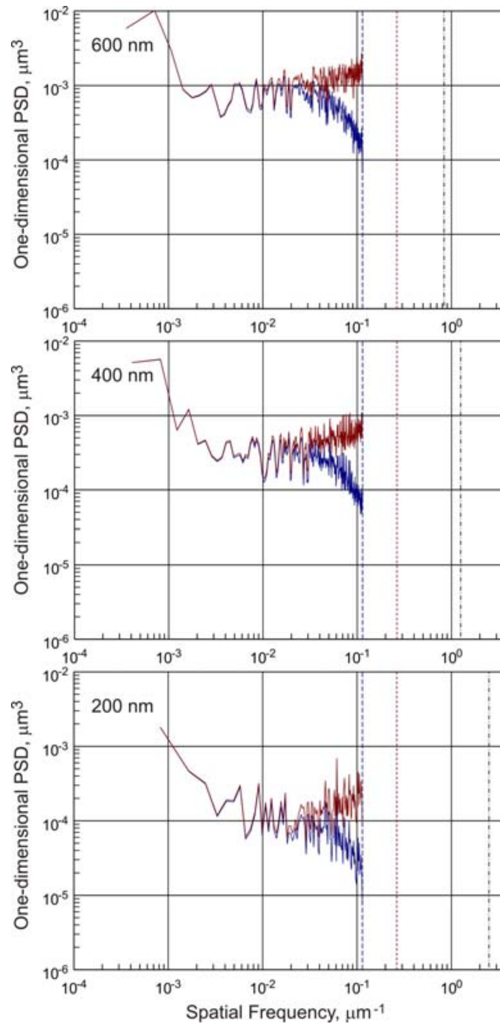

Figure 14: Average 1D PSDs for the 2.5× objective measurements. Excess low frequency noise is due to intrinsic roughness on the wafer. The vertical lines indicate the cutoff frequencies as in Fig. 13. The upturn of the corrected spectra (upper curves) indicates an overestimate of the MTF correction for this objective.

The 20× objective PSD curves in Fig. 13 indicate that the BPRA patterns are matched quite well to the spatial frequency range covered by this objective. The restored spectra are flat, as they should be for the white noise source array. The MTF model parameters appear to give the proper correction factors. The 2.5× objective spectra in Fig. 14 appear to be overcorrected by the nominal MTF correction parameters. The corrected spectra appear to increase at high frequencies, departing from the expected flat white noise spectrum. The reason for this discrepancy is not currently understood. Note that the detector pixel cutoff frequency occurs at a significantly lower spatial frequency than the BPRA feature Nyquist frequency. There is much more high frequency content in these arrays beyond the lens Nyquist frequency in this case than in the 20× objective measurements. Some of that higher frequency content may be aliased back into the lower frequency range, resulting in the upturn at the high frequency end of each corrected spectrum. Another possibility is that the NA value for the 2.5× objective is too small. A larger NA value would move the lens cutoff frequency to a higher value, reducing the amount of the correction in the sampled region below the detector Nyquist frequency. The exact cause of this discrepancy is under investigation.

A measurement with the NewView 20x objective on a polished molybdenum surface is shown in Fig. 15. A typical profile is show in the upper frame. The surface consists of an array of plateaus of various sizes rising above the base level with an average RMS roughness of about 5nm. The nature of this profile is very much like the random telegrapher's signal that has an exponential autocovariance function.[55] The spectrum of such a random process has a $1/f^2$ high frequency dependence, so we can expect the PSD of this surface to follow an inverse-square spatial frequency dependence. This is indeed the case as shown in the lower frame of Fig. 15, where the 1D PSDs for each row in the 640x480 pixel camera field of view are averaged and various MTF corrections applied. The high frequency tail of the corrected curve does indeed have exactly an inverse-square power law dependence (neglecting the aliasing near the Nyquist frequency).

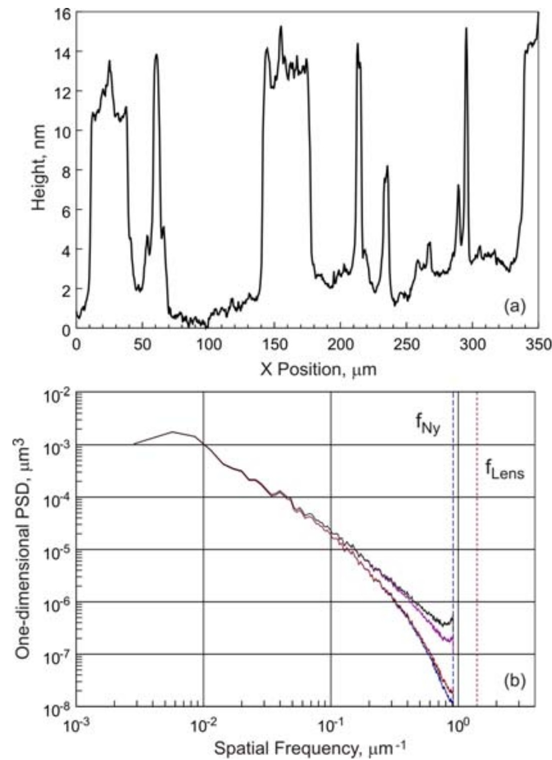

Figure 15: NewView 6300 measurements on a polished molybdenum surface with a 20x objective. A typical surface profile is shown in the upper frame. The average uncorrected PSD is shown as the lowest curve in the bottom frame, with the pixel sampling and objective lens corrections applied individually and then together to give the fully corrected PSD in the upper curve. The location of the objective lens cutoff is indicated to the right of the sensor Nyquist frequency.

6. Discussion and conclusions:

We have investigated in detail a technique, suggested in Refs. [25,26], for precise measurement of the 2D MTF based on use of binary pseudo-random arrays as standard MTF test surfaces. A high-confidence demonstration of the 2D MTF calibration technique has been presented via cross comparison measurements of a number of two dimensional BPR arrays (BPRAs) using two different interferometric microscopes and a scatterometer.

The importance of the MTF calibration has been verified by applying the technique to correct the surface metrology of super polished mirrors performed with the Micromap-570™ and

1 ZYGO NewView ™ -6300 interferometric microscopes. For example, in the Micromap-
2 570™ case, the correction has shown that the spatial frequency bandwidth of the instrument is
3 half of the bandwidth specified based on the detector projected pixel size. Moreover, after the
4 MTF correction, the value of the surface rms roughness increased by a factor of
5 approximately 1.4 even in spite of the fact that it was evaluated over the half of the specified
6 instrumental bandwidth.

7 The investigations performed here and in work [25,26,48,49] have provided experimentally
8 proven arguments for use of the calibration technique based on BPR sequences and arrays as
9 an internationally recognized calibration method for a broad class of surface profilometers.

10 Unlike most conventional test surfaces, the inherent PSD of the BPR gratings and arrays has a
11 deterministic white-noise-like character. This allows the direct determination of the 1D and
12 2D MTF, respectively, with a sensitivity uniform over the entire bandwidth of a profilometer.

13 The BPRA sequences and arrays precisely satisfy the requirement of ease of specification and
14 reproducibility of the test surface when used as a certified standard.

15 The spectral characteristics of the BPR gratings and arrays are mathematically rigorous,
16 reproducible and amenable to simulation, allowing one to *deterministically* construct a
17 sequence (array) with an ideal ('one-bit' wide) autocorrelation function and an absolute step
18 value optimal for a particular instrument.

19 The binary height distributions with two normalized heights, '1' and '0', are easily specified
20 for a number of production processes, including nano- and micro-lithography. For example,
21 an optimized nano-fabrication process described in [49] provides the BPRAs with almost
22 ideal rectangular shape of the elements. The BPRAs have allowed *ab initio* MTF calibration
23 of the interferometric microscopes under investigation in the present work.

24 The distinguishing property of the BPR array is that its PSD spectrum is a result of the
25 distribution of the elements, rather than the element shape. This determines a low sensitivity
26 of the BPRA-PSD spectrum to the shape perturbations demonstrated in [48]. In the presence
27 of fabrication imperfections, the element shape perturbations lead to only a 10-15%
28 perturbation of the inherent PSD of a BPRA. Moreover, it is possible to approximate the
29 perturbation to the inherent PSD [48]. Because the overall magnitude of the BPRG-PSD
30 spectrum is determined by the depth of the grooves, the contribution of the roughness of the
31 substrate can be easily made to be insignificant.

32 In conclusion, the MTF calibration method involving BPR test surfaces can be adapted to a
33 large variety of profiling instruments including interferometers, interferometric microscopes,
34 scanning probe and scanning electron microscopes, scatterometers, etc. For example, existing
35 methods of nano- and micro- lithography are capable of fabrication of BPR surfaces with
36 extremely small (a few nm) and relatively large (dozens and hundreds of microns)
37 fundamental periods suitable for SPMs and large field of view interferometers, respectively.
38 In the case of an SEM, a test BPR sample can be fabricated as a side-cut multilayer coating.
39 The binary character of the multilayer would be provided by use of two materials with
40 different contrast. The material and thickness of a particular layer would be determined from a
41 suitable BPR sequence as a product of the value of an elementary thickness and the number of
42 the repeated identical elements in the sequence. The corresponding developments and
43 experiments are in progress at the Advanced Light Source Optical Metrology laboratory in
44 collaboration with the LBNL Center for X-Ray Optics and the NSLS-II/ BNL optic group.

45 **Acknowledgements**

46 The authors are grateful to Raymond Conley, Mikhail Gubarev, Stefano Marchesini, and
47 Howard Padmore for useful discussions, and Dawn Hilken for nanofabrication. The Advanced

Light Source is supported by the Director, Office of Science, Office of Basic Energy Sciences, Material Science Division, of the U.S. Department of Energy under Contract No. DE-AC02-05CH11231 at Lawrence Berkeley National Laboratory. Research at Brookhaven National Laboratory is sponsored by the U.S. Department of Energy under Contract No. DE-AC02-98CH10886.

Disclaimer

Certain commercial equipment, instruments, or materials are identified in this document. Such identification does not imply recommendation or endorsement by the US Department of Energy, LBNL, BNL, or ALS, nor does it imply that the products identified are necessarily the best available for the purpose.

References

[1] L. Assoufid, O. Hignette, M. Howells, S. Irick, H. Lammert, P. Takacs, “Future metrology needs for synchrotron radiation grazing-incidence optics,” Nucl. Instrum. and Meth. in Phys. Research A **467-468**, 267-70 (2001).

[2] P. Z. Takacs, “X-Ray Mirror Metrology,” in Handbook of Optics, 3rd edition, M. Bass, ed., Vol. V, ch. 46 (in press).

[3] E. L. Church and P. Z. Takacs, “Specification of surface figure and finish in terms of system performance,” Applied Optics **32**(19), 3344-3353 (1993).

[4] G. D. Boreman, *Modulation Transfer Function in Optical and Electro-optical Systems* (SPIE Press, 2001).

[5] R. N. Bracewell, **“**The Fourier Transform and Its Applications,” McGraw-Hill Publishing Company, New York (1986).

[6] J. M. Elson, J. M. Bennett, “Calculation of the power spectral density from surface profile data,” Applied Optics 34(1), 201-208 (201).

[7] V. V. Yashchuk, A. D. Franck, S. C. Irick, M. R. Howells, A. A. MacDowell, W. R. McKinney, “Two dimensional power spectral density measurements of x-ray optics with the Micromap interferometric microscope,” Proceedings of SPIE **5858**, pp. 58580A-1-12 (2005).

[8] V. V. Yashchuk, S. C. Irick, E. M. Gullikson, M. R. Howells, A. A. MacDowell, W. R. McKinney, F. Salmassi, T. Warwick, “Cross-check of different techniques for two dimensional power spectral density measurements of x-ray optics,” Proceedings of SPIE **5921**, pp. 59210G-1-12 (2005).

[9] V. V. Yashchuk, E. M. Gullikson, M. R. Howells, S. C. Irick, A. A. MacDowell, W. R. McKinney, F. Salmassi, T. Warwick, J. P. Metz, T. W. Tonnessen, “Surface roughness of stainless-steel mirrors for focusing soft x rays,” Applied Optics **45**(20), 4833-42 (2006).

[10] E. L. Church, H. A. Jenkinson, and J. M. Zavada, “Relationship between surface scattering and micro-topographic features,” Opt. Eng. **18**(2), 125-36 (1979).

[11] J. C. Stover, “Optical Scattering,” second edition, SPIE Optical Engineering Press, Bellingham (1995).

[12] D. Attwood, “Soft X-rays and Extreme Ultraviolet Radiation,” Cambridge University Press, New York (1999).

1 [13] R. Barakat, "Determination of the optical transfer function directly from the edge
2 spread function," JOSA **55**, 1217 (1965).

3 [14] B. Tatian, "Method for obtaining the transfer function from the edge response
4 function," JOSA **55**, 1014 (1965).

5 [15] K. Creath, "Calibration of Numerical aperture effects in interferometric microscope
6 objectives," *Applied Optics* **28**(15), 3333-8 (1989).

7 [16] P. Z. Takacs, M. X. Li, K. Furenlid, E. L. Church, "Step-height standard for surface-
8 profiler calibration," *Proceedings of SPIE* **1995**, 235-44 (1993).

9 [17] A. Harasaki and J. C. Wyant, "Fringe modulation skewing effect in white-light
10 vertical scanning interferometry," Applied Optics **39**, 2101-6 (2000).

11 [18] G. D. Boreman and S. Yang, "Modulation transfer function measurement using
12 three- and four-bar targets," Appl. Opt. **34**, pp. 8050-8052 (1995).

13 [19] M. Marchywka, D. G. Socker, "Modulation transfer function measurement technique
14 for small pixel detectors," *Applied Optics* **31**(34), 7198-13 (1992).

15 [20] O. P. Nijhawan, P. K. Datta, J. Bhushan, "On the measurement of MTF using
16 periodic patters of rectangular and triangular wave-forms," Nouv. Rev. Optique **6**(1),
17 33-36 (1975).

18 [21] H. G. Rhee, T. V. Vorburger, J. W. Lee, and J. Fu, "Discrepancies between
19 roughness measurements obtained with phase shifting interferometer and white-light
20 interferometry," *Applied Optics* **44**(28) 5919-27(2005).

21 [22] E. Levy, D. Peles, M. Opher-Lipson, and S. G. Lipson, "Modulation transfer function
22 of a lens measured with a random target method," *Applied Optics* **38**(4), 679-83
23 (1999).

24 [23] C. R. Wolfe, J. D. Downie, and J. K. Lawson, "Measuring the spatial frequency
25 transfer function of phase-measuring interferometers for laser optics," *Proceedings of*
26 *SPIE* **2870**, 553-7 (1996).

27 [24] J. F. Song and T. Vorburger, "Standard reference specimens in quality control of
28 engineering surfaces," *J. Res. of the Natl. Inst. Stand. Technol*. **96**, 271 (1991).

29 [25] V. V. Yashchuk, W. R. McKinney, and P. Z. Takacs, "Binary Pseudorandom Grating
30 Standard for Calibration of Surface Profilometers," Optical Engineering **47**(7),
31 073602-1-5 (2008).

32 [26] V. V. Yashchuk, W. R. McKinney, and P. Z. Takacs, "Binary Pseudorandom Grating
33 as a Standard Test Surface for measurement of Modulation Transfer Function of
34 Interferometric Microscopes," Proc. SPIE **6704**, 670408/1-12 (2007).

35 [27] P. H. Bardell, W. H. McAnney, J. Savir, "Built-in test for VLSI pseudorandom
36 techniques," John Wiley and Sons Inc., New York (1987).

37 [28] A. Busboom, H. Elders-Boll, H. D. Schotten, "Uniformly Redundant Arrays,"
38 Experimental Astronomy **8**, 97-123 (1998).

39 [29] B. Sclar, "Digital Communications: Fundamentals and Applications," 2nd Ed.,
40 Prentice Hall, 2001.

41 [30] T. Etzon, "Construction for perfect maps and pseudo-random arrays," *IEEE Trans.*
42 *on Information Theory* **34**(5), 1308-16 (1988).

[31] D. D. Koleske, and S. J. Sibener, "Generation of pseudo-random sequence for use in cross-correlation modulation," *Rev. Sci. Instrum.* **63**(8), 3852-5 (1992).

[32] A. Mitra, "On Pseudo-Random and orthogonal Binary Spreading Sequences," Int. J. Information Techn. **4**(2), 137-144 (2008).

[33] W.T. Chu, "Impulse-Response and Reverberation-Decay Measurements Made by Using a Periodic Pseudorandom Sequence," Applied Acoustics **29**, 193-205 (1990).

[34] T.E. Stern, A. Blaquiere, J. Valat, "Reactivity Measurement Using Pseudo-Random Source Excitation," J. Nucl. Energy, Pt. A and B, **16**, 499 (1962).

[35] J. Gordon, N, Kroo, G. Orban, L. Pal, P. Pellionisz, F. Szlavik, I. Vizi, "Correlation Type Time-of-Flight Spectrometer with Magnetically Pulsed Polarized Neutrons," Phys. Letters **26A**, 122 (1968).

[36] K. Skold, "A Mechanical Correlation Chopper for Thermal Neutron Spectroscopy," Nucl. Instr. and Meth. **63**, 114-16 (1968).

[37] A. Virjo, "Statistical Analysis of Cross-Correlation Chopper for Time-of-Flight Measurements," Nucl. Instr. and Meth. **63**, 351-352 (1968).

[38] A. Virjo, "The Fourier method in Slow neutron time-of-flight Spectrometry with a Pseudo-Random Input Signal," Nucl. Instr. and Meth. **73**, 189-99 (1969).

[39] A. Virjo, "Slow Neutron Time-of-Flight Spectrometry with a Pseudo-Random Input Signal," Nucl. Instr. and Meth. **75**(1), 77-84 (1969).

[40] V. L. Hirschy, and J. P. Aldridge, "A Cross Correlation Chopper for Molecular Beam Modulation," *Rev. Sci. Instrum.* **42**(3), 381-3 (1971).

[41] G. Comsa, R. David, and B. J. Schumacher, "Magnetically suspended cross-correlation chopper in molecular beam-surface experiments," *Rev. Sci. Instrum.* **52**(6), 789-91 (1981).

[42] V. V. Yashchuk, B. N. Ashkinadzi, M. N. Groshev, V. F. Ezhov, T. A. Isaev, V. A. Knyazkov, G. B. Krygin, V. L. Ryabov, "Cross-Correlation Time-of-Flight Spectrometer of Gas-Dynamic Molecular Beams," *Instruments and Experimental Techniques* **40**(4), 501 (1997).

[43] S. M. Kay, "Modern Spectral Estimation: Theory and Application," Prentice Hall, Englewood Cliffs (1988).

[44] Fenimore, E. E. and Cannon, T. M., "Coded aperture imaging with uniformly redundant arrays," Appl. Opt. **17**(3), 337-47 (1978).

[45] E. Caroli, J. B. Stephen, G. Di Cocco, L. Natalucci, A. Spizzichino, "Coded aperture imaging in x- and gamma-ray astronomy," *Space Science Reviews* **45**, 349-403 (1987).

[46] Marchesini, S., Boutet, S., Sakdinawat, A. E., Bogan, M. J., Bajt, S., Barty, A., Chapman, H. N., Frank, M., Hau-Riege, S. P., Szöke, A., Cui, C., Shapiro, D. A., Howells, M. R., Spence, J. C. H., Shaevitz, J. W., Lee, J. Y., Hajdu, J., and Seibert, M. M., "Massively parallel X-ray holography," Nat. Photonics 2, 560–563 (2008).

[47] E. H. Anderson, "Specialized electron beam nanolithography for EUV and X-ray diffractive optics," IEEE J. Quant. Elect. **42**, 27-35 (2006).

[48] S. K. Barber, P. Soldate, E. H. Anderson, R. Cambie, S. Marchesini, W. R. McKinney, P. Z. Takacs, D. L. Voronov, V. V. Yashchuk, "Binary Pseudo-random Gratings and Arrays for Calibration of the Modulation Transfer Function of

1 Surface Profilometers: Recent Developments," Proc. SPIE **7448**, 744802/1-12
2 (2009).

3 [49] S. K. Barber, P. Soldate, E. Anderson, R. Cambie, W. R. McKinney, P. Z. Takacs,
4 D. L. Voronov, V. V. Yashchuk, *Development of Pseudo-random Binary Gratings*
5 *and Arrays for Calibration of Surface Profile Metrology Tools,* 53rd International
6 Conference on Electron, Ion and Photon Beam Technology and Nanofabrication –
7 EIPBN (Marco Island, Florida, United States, May 26-29, 2009).

8 [50] J. Rifkin, K. A. Klicker, D. R. Bjork, D. R. Cheever, T. F. Schiff, J. C. Stover,
9 Cady, M. Fredrick D. J. Wilson, P. D.Chausse, K. H. Kirchner, "Design Review of a
10 Complete Angle Scatter Instrument," Proc. SPIE **1036**, 116 (1988).

11 [51] The Scatter Works, Inc.; http://www.thescatterworks.com.

12 [52] J. W. Goodman, "Introduction to Fourier Optics," third edition, Roberts & Company
13 Publishers, Englewood (2005).

14 [53] E. L. Church, P. Z. Takacs, "Effects of optical transfer function in surface-profile
15 measurements," *Proceedings of SPIE* **1164**, 46-59 (1989).

16 [54] The mirror was supplied for the tests by Mikhail Gubarev.

17 [55] A. Papoulis, "Probability, Random Variables, and Stochastic Processes," McGraw-
18 Hill, Inc., New York, (1965).